Analytical Model of a Bearingless Motors With Conformal Mapping Method

Zikai YANG*, Zeqiang HE** and Jiahao CHEN*
* School of Information Science and Technology, ShanghaiTech University
China
** Department of Mechanical Engineering, Institute of Science Tokyo
Japan

Abstract
This paper presents an analytical framework for modeling the air-gap magnetic field, suspension force, and Maxwell stress tensor (MST) in bearingless permanent magnet synchronous motors (BPMSMs), with the goal of improving both suspension performance evaluation and early-stage design efficiency. By leveraging Schwarz–Christoffel conformal mappings, we derive closed-form solutions for the magnetic field in the air gap without assuming infinite slot depth. The model naturally accommodates slot-depth effects and captures spatial harmonics critical to MST and force evaluation. The analytical solution is embedded within a multi-objective optimization loop, reducing the time of a single evaluation from hours to under one minute. Furthermore, we propose a unified visualization method combining MST contours, radial force fields, and error-angle loci, which enables intuitive interpretation of suspension stability. The analytical results show strong agreement with finite element analysis (FEA), confirming the model's validity. The proposed method significantly reduces computational effort while maintaining accuracy, making it suitable for design space exploration. Future work will address magnetic saturation and rotor slotting to further enhance model fidelity.

Keywords : Bearingless Motor, Analytical Model, Schwarz-Chritoffel Mapping, Finite Element Analysis, Suspension Force, Maxwell Stress Tensor

1. Introduction

Bearingless motors possess unique friction-free and seal-free advantages that make them superior to conventional motors in applications such as compressors [1], cooling fans [2], and implantable medical devices [3]. This manuscript focuses on the left ventricular assist device (LVAD) blood pump in implantable medical devices [4], specifically addressing the requirements of miniaturization and high reliability.

Despite unique advantages, optimizing the design of bearingless motors for maximum performance necessitates the finite element analysis. While FEA delivers high-fidelity representations of complex geometries and magnetic material nonlinearity, its reliance on mesh generation and repeated numerical solves incurs substantial computational overhead, hindering rapid design optimization. In contrast, analytical models can drastically reduce computation time while still providing closed-form insights into how design parameters affect machine performance. Among these, conformal mapping techniques stand out for their ability to transform complex slot and pole geometries into simpler canonical domains, where boundary value problems admit quasi-analytical solutions.

Zhu et al. [5] first introduce a permeance function of the airgap to derive magnetic reluctance distributions with considering the slotted stator. Zarko et al. [6] extended this framework by formulating a complex-reluctance approach for more general slot shapes. The development of the Schwarz–Christoffel Toolbox by and subsequent work by Tobin A. Driscoll [7] further automated polygonal mapping procedures. Conformal mapping has since been successfully applied to surface-mounted permanent-magnet (SPM) motors, flux-reserve bearing designs, and a variety of other rotating-field devices.

In this work, we adapt the conformal mapping paradigm specifically to bearingless motors. Our contributions are threefold:

By formulating the mapping directly in the air gap cross section, our method dispenses with the infinite-slot-depth assumption and explicitly captures how variations in slot depth modulate the magnetic field; Embedding the analytical model within a multi-objective optimization framework compresses single-point evaluation times from hours to under one minute, facilitating rapid design exploration; We propose a unified visualization scheme—combining Maxwell stress tensor contours, radial suspension force fields, and error angle calculation—that enables designers to immediately assess stability and control trade-offs.

By integrating these advances, our framework offers a fast, accurate, and interpretable tool for the early-stage optimization of bearingless machines.

2. Conformal Mapping for Chosen Motor

This section presents the conformal mapping approach. For slotless machines, the air gap flux density distribution has been extensively studied under simple boundary conditions [8]. Once stator or rotor slots are introduced, however, the air gap geometry becomes nonconcentric and the resulting boundary-value problem grows highly complex. In the analytical modeling of bearingless motors, where slotting effects must be accounted for. This complexity makes conformal mapping indispensable.

Conformal mapping is a technique from complex analysis that carries a complex polygonal domain into a simpler canonical region via an analytic, angle-preserving, and invertible function. By exploiting this property, we can transform the original slotted air gap cross-section into a slotless rectangle or a circular annulus, reducing the problem to solving Laplace's equation in a regular geometry.

For bearingless machines, we are primarily concerned with the suspension force and the performance of the Maxwell stress tensor in the air-gap magnetic field. Therefore, we focus on the field distribution along the middle of the air gap, which is a source-free region where the governing equation reduces to Laplace's equation.

When evaluating the magnetic flux density along the air-gap midline, most higher-order harmonics generated by currents inside the slots are largely filtered out. Consequently, the dominant contributor of the Maxwell stress tensor in the air gap is the stator surface current density, which can be accessed to derive the Maxwell stress tensor. The deviation of the MST depends on the exponential transformation, which transfers a cylinder region into a square area, enabling an analytic solution of the MST. However, in the presence of slotted stators or rotors, the air gap region becomes doubly connected, and the cylinder assumption of the air gap is destroyed.

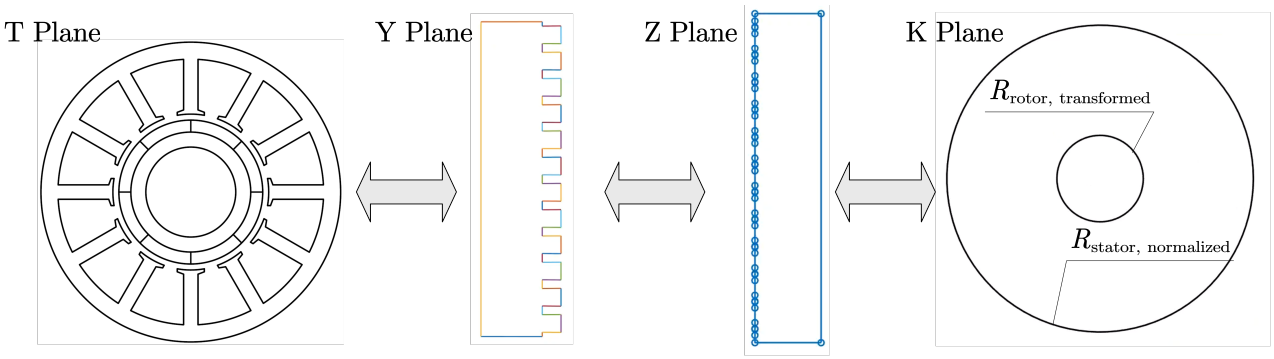

Fig. 1: Basic mapping procedure from an example motor.

To derive an analytic solution, we perform the following sequence of transformations on the machine's air gap domain:

Assuming that the origin motor cross-section as the T plane, we adopted the three conformal mapping method below in sequence to map the slotted motor in T plane into the slotless motor in K plane.

$$Y = \ln T, \quad Z = z_0 + c \int_{z_0}^{z} \prod_{j=1}^{n-1} \left(Y - Y_j\right)^{\alpha_j - 1} \mathrm{d}Y, \quad K = e^{\frac{2\pi}{F}\left(Z - \frac{F}{2}\right)} \tag{1}$$

where T, Y, Z, K are complex variables in their plane, Y_j and α_j are vertixes and interior angles at the vertices,

z_0 is a constant to move the transformed rectangular to the positive half plane in Z plane, E, F are the length and width of the rectangle, respectively, c denotes the constant of the Schwarz–Christoffel transformation.

Fig. 1 shows the mapping procedure for the chosen motor. For the mappings under consideration, the logarithmic transform, the Schwarz–Christoffel transform, and the exponential transform respectively, all are conformal and invertible.

2.1. Logarithmic Mapping

$$Y = \ln T \tag{2}$$

Eq. 2 maps the original motor geometry in the T plane to a slotted rectangle in the Y plane. Note that if both stator and rotor feature slots, we apply the same simplification: a current density distribution along the slot openings, with slot depth set equal to that of the original machine.

2.2. Schwarz-Christoffel Mapping

$$Z = z_0 + c \int_{z_0}^{z} \prod_{j=1}^{n-1} \left(Y - Y_j\right)^{\alpha_j - 1} \mathrm{d}Y \tag{3}$$

Eq. 3 transforms the slotted rectangle in the Y plane into a slotless rectangle in the Z plane. This step greatly simplifies the computation [9] and adjusts the relative positions of stator and rotor.

2.3. Exponential Mapping

$$K = e^{\frac{2\pi}{F}\left(Z - \frac{E}{2}\right)} \tag{4}$$

Eq. 4 converts the slotless rectangle in the Z plane into a slotless circular annulus in the K plane. Care must be taken here to map the stator and rotor back to their original relative positions.

2.4. Transformation for potential function and density function

We take the line current density distributed on the stator and rotor in the T plane as the excitation for the air gap field. Our line source possesses the following characteristics:

$$\begin{aligned} J_{\mathrm{T}} &= K_{\mathrm{T}}(\alpha) \cdot \delta_{\mathrm{T}}(r, \alpha) \\ J_{\mathrm{K}} &= K_{\mathrm{K}}(\alpha) \cdot \delta_{\mathrm{K}}(r, \alpha) \cdot |f'(T)| \end{aligned}$$

where r, α denote the radial and angular coordinates in the complex plane (i.e., the polar-coordinate variables); $f(T)$ is the conformal mapping function that carries points from the T plane into the K plane; J represents the strength (or magnitude) of each line source; $K(\cdot)$ is the spatial distribution function of those line sources; A is the scalar potential function whose gradient yields the magnetic field; $\delta(r, \alpha)$ is a two-dimensional impulse function in a certain plane.

Through the propoerties of the coonformal mapping, it is then straightforward to derive that the resulting magnetic potential function exhibits these properties:

$$\begin{aligned} \nabla_{\mathrm{T}}^2 A_{\mathrm{T}}(T) &= \frac{1}{|f'(T)|^2} \nabla_{\mathrm{K}}^2 A_{\mathrm{K}}(K) \\ \nabla_{\mathrm{T}}^2 A_{\mathrm{T}}(T) &= -\mu_0 K_s \delta_{\mathrm{T}}(\alpha) \\ \Rightarrow \nabla_{\mathrm{K}}^2 A_{\mathrm{K}}(K) &= -\mu_0 K_s \delta_{\mathrm{K}}(\alpha) \cdot |f'(T)| \end{aligned} \tag{5}$$

where A denotes the potential function, μ_0 is the vacuum permeability. Also the magnetic field B in K plane satisfies Eq. 6.

$$\begin{bmatrix} B_{nK} \\ B_{tK} \end{bmatrix} = |f'(T)| \begin{bmatrix} B_{nT} \\ B_{tT} \end{bmatrix} \tag{6}$$

3. Air Gap Flux Density

3.1. Assumptions

Without losing the physical properties, we first make the following assumptions:

- The iron core has infinite permeability and the permanent magnets have permeability same as air;
- All magnetic materials behave linearly;
- Adopt the simplier stator and rotor geometries.

3.2. The field excited by PM

The equivalent circuit excited by PM can be obtained as [10]:

$$\begin{aligned} M_r &= \sum_{n=1,3,5\ldots} M_n \sin\left(np\left(\alpha-\Theta\right)\right) \\ M_n &= \frac{4B_{rem}}{\mu_0 n\pi}\sin\frac{n\pi}{2}\sin\frac{n\pi\alpha}{2} \\ J_{\mathrm{PM}}\left(\alpha\right) &= \sum_n \frac{b_n}{\mu_0}\sin\left(n\alpha-\Theta\right) \end{aligned} \tag{7}$$

where

$$\begin{aligned} b_n &= k_n\cdot\left(R_r^{np+1}-\frac{np+1}{2}R_r^{2np}R_m^{1-np}+\frac{np-1}{2}R_m^{1-np}\right) \\ k_n &= \begin{cases} -\frac{\mu_0 M_1}{2}\ln r, np=1 \\ \frac{\mu_0 np M_n}{(np)^2-1}, np\neq 1 \end{cases} \end{aligned} \tag{8}$$

In the above expressions, M_r denotes the permanent-magnet magnetization function, where M_n is its amplitude of the n-th harmonic; R_r, R_m and R_s are the rotor iron outer radius, the permanent magnet (PM) outer radius, and the stator-inner radius, respectively; p is the number of pole pairs of PMs.

Apply the conformal mapping mentioned in Section 2, we can transform the linear current source into a slotless plane as Fig. 8. The magnetic potential function in the air gap satisfies the governing equation in the form of Lapalace equation. The governing equation and the boundary condition in the slotless plane are given by:

$$\begin{aligned} \nabla^2 A &= 0 \\ \frac{\partial A_{\mathrm{PM}}}{\partial r}\Big|_{r=R_r^K} &= \mu_0 J_{\mathrm{PM}},\ \frac{\partial A_{\mathrm{PM}}}{\partial \alpha}\Big|_{r=R_s^K}=0 \end{aligned} \tag{9}$$

where the superscript K denotes the corresponding plane of the physical quantity, A denotes the magnetic vector potential [11].

Here, the current density function J_{PM} holds the Eq. 5, which means that the current density in T plane can be transformed to K plane through the series of conformal mapping:

$$J_{\mathrm{PM}}^K = J_{\mathrm{PM}}^{\mathrm{T}}\cdot\left|f'\left(T\right)\right| \tag{10}$$

By applying the method of separation of variables, one can derive closed-form expressions for the radial and tangential components of the magnetic flux density in the slotless region as follows:

$$\begin{aligned} B_{n\mathrm{PM}} &= \sum_n \mu_0 \frac{r^{n-1}+R_s^{2n}r^{-n-1}}{R_r^{n-1}-R_s^{2n}R_r^{-n-1}}\left(J_{\mathrm{PM}\cos}\sin\left(n\alpha\right)-J_{\mathrm{PM}\sin}\cos\left(n\alpha\right)\right) \\ B_{t\mathrm{PM}} &= \sum_n \mu_0 \frac{r^{n-1}-R_s^{2n}r^{-n-1}}{R_r^{n-1}-R_s^{2n}R_r^{-n-1}}\left(J_{\mathrm{PM}\sin}\sin\left(n\alpha\right)+J_{\mathrm{PM}\cos}\cos\left(n\alpha\right)\right) \end{aligned} \tag{11}$$

From equation 6 and 1, we can obtain the flux density distribution in the primary plane.

3.3. The field excited by stator coil

We take the stator torque winding magnetomotive force (MMF) as an example to describe the calculation procedure of the stator winding. Given $\mathcal{F}$ as the stator winding function of the example motor, then we have:

$$J_s = \frac{\mathcal{F}}{b_0 \cdot R_s} \cdot \delta(r, \alpha) \tag{12}$$

where b_0 is the slot open length of the stator.

By treating the current density distributed on the stator surface as the source of the air gap field, we obtain the stator current density expression corresponding to the MMF as above. By then applying the conformal mapping introduced in Section 2, this current density distribution can be mapped into the slotless plane.

When calculating the air-gap magnetic field distribution of the torque windings, the rotor surface is assumed to have zero surface current distribution, while the stator surface current density distribution is determined using MMF calculations. Under these conditions, the air gap potential function satisfies the governing equation in the form of Lapalace equation.

$$\begin{aligned} &\nabla \times \nabla \times A = 0 \\ &\frac{\partial A}{\partial r} \mid_{r=R_s^{\mathrm{K}}} = \mu_0 J^{\mathrm{K}}, \quad \frac{\partial A}{\partial \alpha} \mid_{r=R_r^{\mathrm{K}}} = 0 \end{aligned} \tag{13}$$

where the superscript K denotes the corresponding plane of the physical quantity, A denotes the magnetic vector potential.

Here, the current density function J^{K} holds the Eq. 5, which means that the current density in T plane can be transformed to K plane through the series of conformal mapping

$$J_w^K = J_w^{\mathrm{T}} \cdot |f'(T)| \tag{14}$$

By applying the method of separation of variables, one can derive closed-form expressions for the radial and tangential components of the magnetic flux density in the slotless region as follows:

$$\begin{aligned} B_{nw} &= \sum_n \mu_0 \frac{r^{n-1} + R_r^{2n} r^{-n-1}}{R_s^{n-1} - R_r^{2n} R_s^{-n-1}} \left(J_{\mathrm{PM}\cos} \sin(n\alpha) - J_{\mathrm{PM}\sin} \cos(n\alpha)\right) \\ B_{tw} &= \sum_n \mu_0 \frac{r^{n-1} - R_r^{2n} r^{-n-1}}{R_s^{n-1} - R_r^{2n} R_s^{-n-1}} \left(J_{\mathrm{PM}\sin} \sin(n\alpha) + J_{\mathrm{PM}\cos} \cos(n\alpha)\right) \end{aligned} \tag{15}$$

From equation 6 and 1, we can obtain the flux density distribution in the primary plane.

3.4. Force performance

Based on the above process, we can obtain the air gap magnetic flux density. The MST and suspension force of the motor are given by [3]

$$\begin{aligned} \overrightarrow{\sigma} = \begin{bmatrix} \sigma_{\mathrm{n}} \\ \sigma_{\mathrm{t}} \end{bmatrix} &= \begin{bmatrix} \frac{1}{2\mu_0}\left(B_n^2 - B_t^2\right) \\ \frac{1}{\mu_0} B_n B_t \end{bmatrix} \\ \begin{bmatrix} F_x \\ F_y \end{bmatrix} &= \begin{bmatrix} \int_S \overrightarrow{\sigma} \cdot \hat{x} \mathrm{d}S \\ \int_S \overrightarrow{\sigma} \cdot \hat{y} \mathrm{d}S \end{bmatrix} \end{aligned} \tag{16}$$

As for the bearingless permanent magnet synchronous motor, we can simplify the Eq. 16 into more detailed form:

$$\begin{aligned} F_x &= \sigma_S V_R \frac{1}{p_s \delta_e} \cos\left[\phi_0 - \Theta\right] + \sigma_S V_R \frac{1}{r} \cos\left[\phi_0 - \Theta\right] \\ F_y &= \sigma_S V_R \frac{1}{p_s \delta_e} \sin\left[\phi_0 - \Theta\right] + \sigma_S V_R \frac{1}{r} \sin\left[\phi_0 - \Theta\right], \\ \sigma_S &= \frac{\hat{B}_m \hat{A}_S}{2}. \end{aligned} \tag{17}$$

where $\hat{B}_m$, $\hat{A}_S$ are amplitude of the magnetic and eletrical loading, respectively, V_R is the rotor volumn, p_s denotes the pole-pairs of the suspension winding, r presents the airgap radius, Θ is the rotor position, ϕ_0 is the phase of suspension winding, which can be regarded as the force angle of the suspension winding.

4. Result

To validate the proposed analytical framework, a bearingless permanent-magnet synchronous machine (BPMSM) was selected as the test case. Its key geometric and electromagnetic parameters are summarized in Table 1. Figures 3a-5a compare the air gap flux density distributions computed by the analytical model against those obtained from finite element analysis. The close agreement across all machine regions confirms the accuracy of the conformal mapping approach.

Table 1: Parameters of the chosen motor

Parameters	Symbol	Design values
Number of stator slots	Q_s	24
Number of rotor poles(PMs)	p	8
Pole number of suspension winding	p_s	10
Inner radius of stator	R_s	26 mm
Outer radius of rotor	R_r	20 mm
Outer radius of PMs	R_{PM}	24 mm
PM arc angle	α_{PM}	45 degree
Length of the inner air gap	g	2 mm
Stack length	l_{ef}	15 mm
PM remanent flux density	B_{rem}	1.2 T

For bearingless motor, we adopt the dual-purpose no voltage winding (DPNV) [12], the current connection diagram is below:

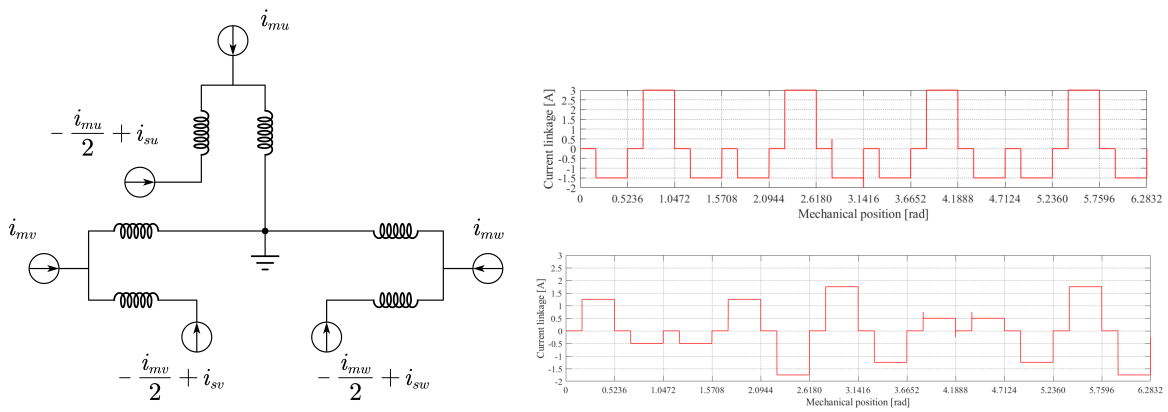

(a) (b)

Fig. 2: The configuration of dual-purpose no voltage winidng (a) and the MMF produced by the winding (b).

In this circuit, the magnitude of torque and suspension winding current is set as:

$$i_{mu} = 1\mathrm{A}, i_{mv} = i_{mw} = -0.5\mathrm{A} \tag{18}$$

$$i_{su} = 0.2\mathrm{A}, i_{sv} = i_{sw} = -0.05\mathrm{A} \tag{19}$$

Therefore we can obtain the flux density in the air gap, compared with the FEA results in Fig. 3-5.

From these results, we observe that, aside from minor discrepancies in the magnetic field at a few individual stator teeth, the flux density closely matches the FEA predictions.

Fig. 6 shows the variation in the density function before and after the conformal mapping. As can be seen, the density function exhibits more pronounced magnetic field distortion at the slot openings after the transformation, while the overall distribution remains essentially unchanged.

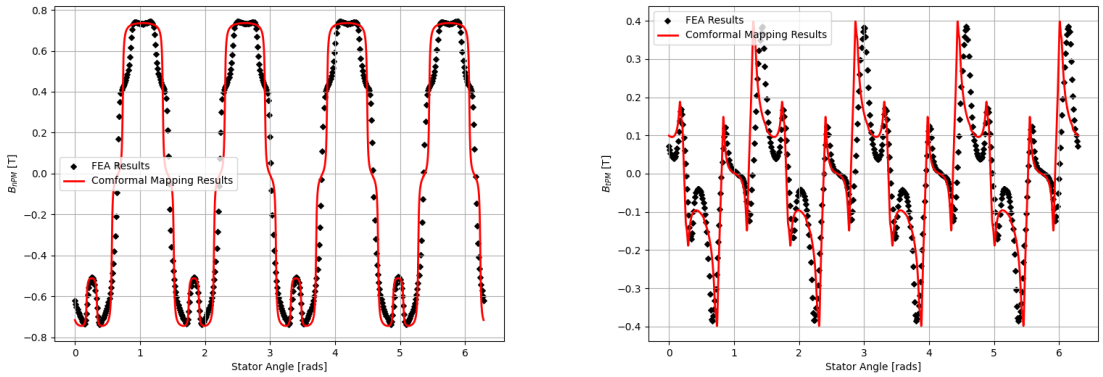

(a) (b)

Fig. 3: The normal (a) and tangential (b) component of the air gap flux density excited by permanent magnet.

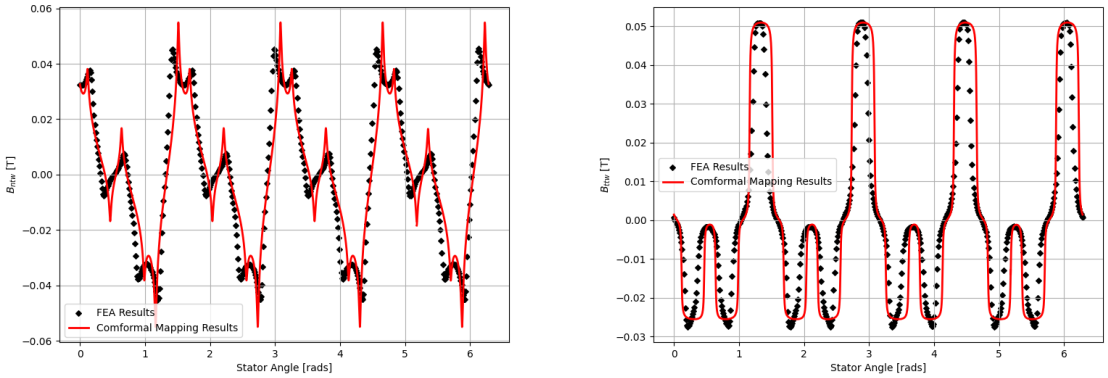

(a) (b)

Fig. 4: The normal (a) and tangential (b) component of the air gap flux density excited by torque widning.

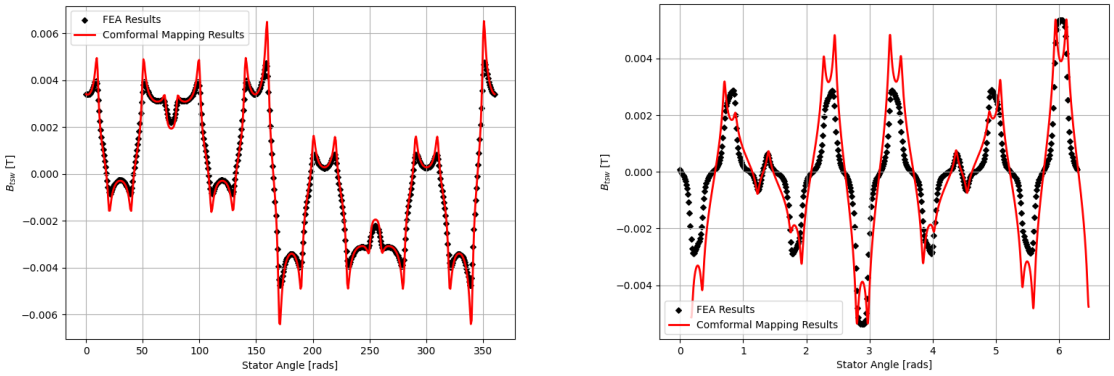

(a) (b)

Fig. 5: The normal (a) and tangential (b) component of the air gap flux density excited by suspension widning.

Then we set the suspension current pahse to 45°, the Maxwell stress tensor and the suspension force along the air gap is shown in Fig. 7 and Fig. 8.

In these figures, the suspension force error angle is defined as the actual angle of the suspension force and the desired suspension force. Through the figures it can be observed that the suspension force contains substantial

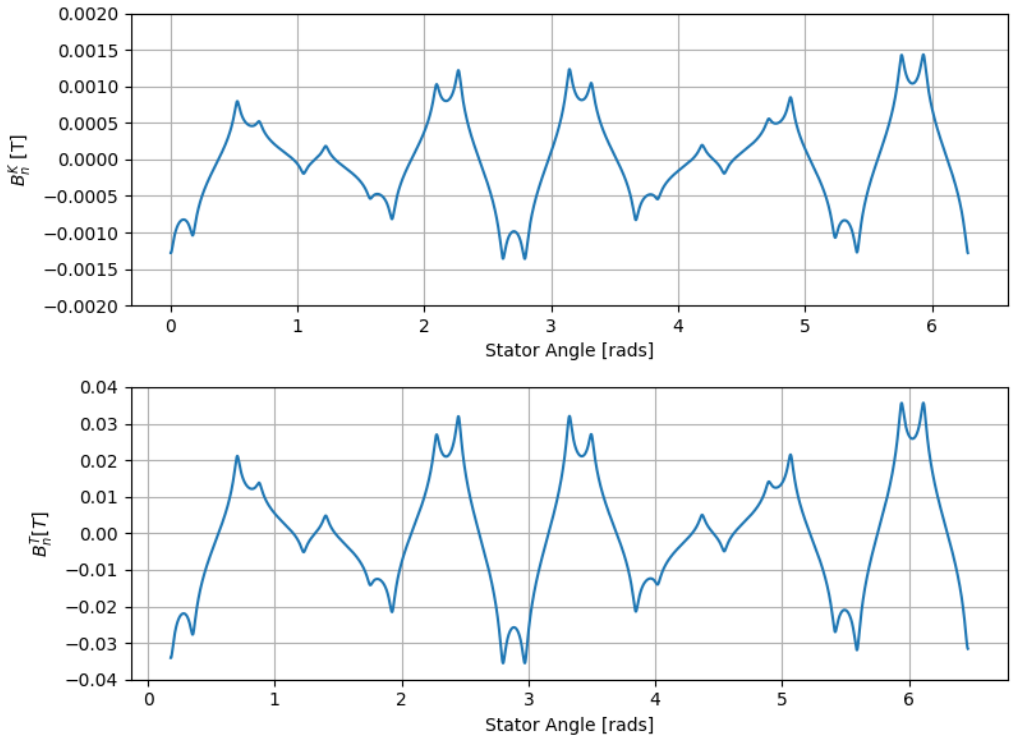

Fig. 6: The computed density function in the air gap in K plane (B_n^K) and T plane (B_n^T).

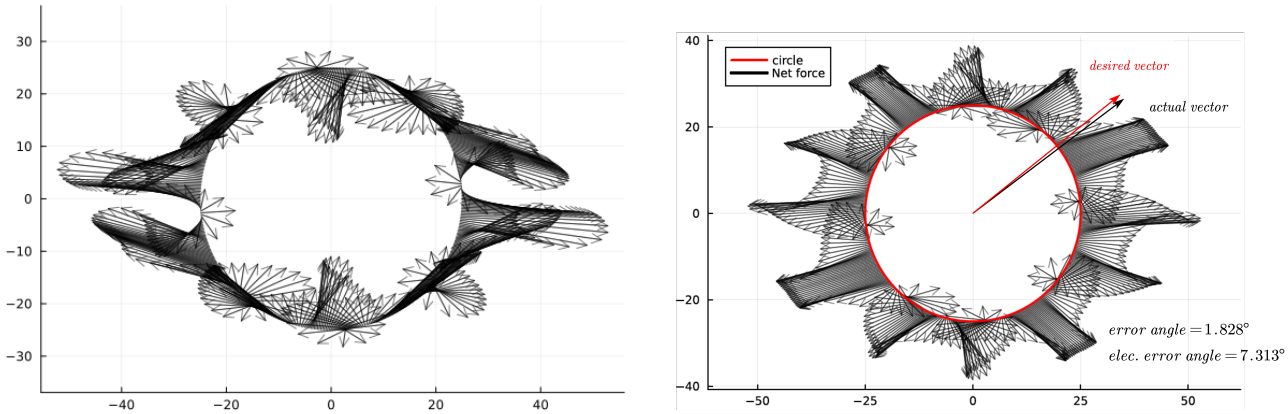

(a) The MST along the air gap calculated by proposed method. (b) The force along the air gap calculated by proposed method.

Fig. 7: Air gap MST and suspension force distribution under field calculated by proposed method.

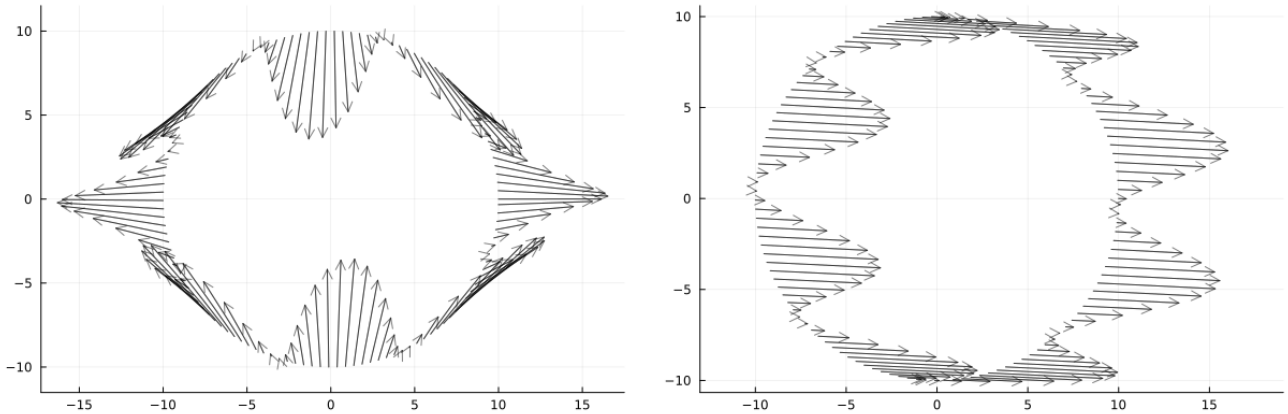

(a) The MST along the air gap.

(b) The suspension force along the air gap in x-axis.

Fig. 8: Air gap MST and suspension force distribution under the fundamental harmonic field ($p = 4$).

higher-order harmonic components along the air gap. Compared to the pure fundamental component, when the measured suspension-force profile more closely approximates the ideal circular distribution of the fundamental (i.e., exhibits low harmonic distortion), the machine is more likely to achieve superior suspension performance. In other words, a smaller error angle, corresponds to a more uniform, stable suspension force.

Furthermore, when computing the air gap magnetic field distribution, the suspension force profile, and the Maxwell stress tensor along the gap, the computational burden of a FEA scales directly with the size and sparsity of the mesh generated system matrices. In contrast, in our analytical approach the dominant cost lies in evaluating the Schwarz–Christoffel mapping. Crucially, for a rotor without slots—meaning the machine's reluctance profile does not change with angular position—the Schwarz–Christoffel mapping coefficients need only be computed once for all rotor angles. Even in the case of a doubly-salient machine, the Schwarz–Christoffel mapping coefficients for any given rotor position need only be computed once. Subsequent field and force calculations then reuse that single mapping, delivering a dramatic reduction in compute time compared to FEA, where one must rebuild and solve a new mesh at each angular increment.

5. Conclusion

This paper develops an efficient analytical framework for air gap field, suspension force, and Maxwell stress tensor computations in bearingless machines by leveraging Schwarz–Christoffel conformal mappings. Although this modeling approach relies on several simplifying assumptions, it has been shown to agree closely with FEA results while drastically reducing evaluation time. We have also introduced new visualization techniques for suspension forces and Maxwell stress tensor distributions.

Our next step is to integrate these analytical and visualization tools with existing performance metrics into a unified framework for assessing bearingless motor suspension performance. Going forward, we will extend the model to include magnetic saturation effects and to quantify how slotting further modulates both the suspension forces and the air gap field.

References

[1] D. Eaton, J. Rama, and S. Singhal, "Magnetic bearing applications and economics," in 2010 Record of Conference Papers Industry Applications Society 57th Annual Petroleum and Chemical Industry Conference (PCIC), 2010, pp. 1–9.

[2] H. Sugimoto, I. Shimura, and A. Chiba, "Principle and test results of energy-saving effect of a single-drive bearingless motor in cooling fan applications," IEEJ Journal of Industry Applications, vol. 6, no. 6, pp. 456–462, 2017.

[3] J. Chen, J. Zhu, and E. L. Severson, "Review of bearingless motor technology for significant power applications," IEEE Transactions on Industry Applications, vol. 56, no. 2, pp. 1377–1388, 2020.

[4] J. D. Schmitto, J. S. Hanke, S. V. Rojas, M. Avsar, and A. Haverich, "First implantation in man of a new magnetically levitated left ventricular assist device (heartmate iii)," The Journal of Heart and Lung Transplantation, vol. 34, no. 6, pp. 858–860, 2015.

[5] Z. Zhu and D. Howe, "Instantaneous magnetic field distribution in permanent magnet brushless dc motors. iv. magnetic field on load," IEEE Transactions on Magnetics, vol. 29, no. 1, pp. 152–158, 1993.

[6] D. Zarko, D. Ban, and T. Lipo, "Analytical calculation of magnetic field distribution in the slotted air gap of a surface permanent-magnet motor using complex relative air-gap permeance," IEEE Transactions on Magnetics, vol. 42, no. 7, pp. 1828–1837, 2006.

[7] T. A. Driscoll, "Schwarz-christoffel toolbox user's guide," Tech. Rep., 2005.

[8] K. J. Binns and P. J. Lawrenson, Analysis and computation of electric and magnetic field problems: pergamon international library of science, technology, engineering and social studies. Elsevier, 2013.

[9] P. Jalali, S. T. Boroujeni, and N. Bianchi, "Analytical modeling of slotless eccentric surface-mounted pm machines using a conformal transformation," IEEE Transactions on Energy Conversion, vol. 32, no. 2, pp. 658–666, 2017.

[10] S. T. Boroujeni and H. B. Naghneh, "Analytical modelling and prototyping a slotless surface-inset pm machine," IET Electric Power Applications, vol. 11, no. 3, pp. 312–322, 2017. [Online]. Available: https://ietresearch.onlinelibrary.wiley.com/doi/abs/10.1049/iet-epa.2016.0402

[11] L. Wu, Z. Zhu, D. Staton, M. Popescu, and D. Hawkins, "Analytical prediction of electromagnetic performance of surface-mounted pm machines based on subdomain model accounting for tooth-tips," IET Electric Power Applications, vol. 5, pp. 597–609, 2011. [Online]. Available: https://digital-library.theiet.org/doi/abs/10.1049/iet-epa.2010.0271

[12] E. L. Severson, R. Nilssen, T. Undeland, and N. Mohan, "Design of dual purpose no-voltage combined windings for bearingless motors," IEEE Transactions on Industry Applications, vol. 53, no. 5, pp. 4368–4379, 2017.